Acta Oceanol. Sin., 2022, Vol. 41, No. 11, P. 1–11
https://doi.org/10.1007/s13131-021-1945-5
http://www.aosocean.com
E-mail: ocean2@hyxb.org.cn

Intra-seasonal variability of the abyssal currents in COMRA's contract area in the Clarion-Clipperton Zone

Fangfang Kuang[1], Jing Cha[1], Junpeng Zhang[1]*, Aijun Pan[1], Hangyu Chen[1], Xiwu Zhou[1], Chunsheng Jing[1], Xiaogang Guo[1]

[1] Third Institute of Oceanography, Ministry of Natural Resources, Xiamen 361005, China

Received 3 May 2021; accepted 12 July 2021

Abstract

In this paper, the intra-seasonal variability of the abyssal currents in the China Ocean Mineral Resources Association (COMRA) polymetallic nodule contact area, located in the western part of the Clarion and Clipperton Fraction Zone in the tropical East Pacific, is investigated using direct observations from subsurface mooring instruments as well as sea-surface height data and reanalysis products. Mooring observations were conducted from September 13, 2017 to August 15, 2018 in the COMRA contact area (10°N, 154°W). The results were as follows: (1) At depths below 200 m, the kinetic energy of intra-seasonal variability (20–100 d) accounts for more than 40% of the overall low-frequency variability, while the ratio reaches more than 50% below 2 000 m. (2) At depths below 200 m, currents show a synchronous oscillation with a characteristic time scale of 30 d, lasting from October to the following January; the energy of the 30-d oscillation increases with depth until the layer of approximately 4 616 m, and the maximum velocity is approximately 10 cm/s. (3) The 30-d oscillation of deep currents is correlated with the tropical instability waves in the upper ocean.

Key words: intra-seasonal variability, abyssal currents, Clarion-Clipperton Zone, tropical instability waves

Citation: Kuang Fangfang, Cha Jing, Zhang Junpeng, Pan Aijun, Chen Hangyu, Zhou Xiwu, Jing Chunsheng, Guo Xiaogang. 2022. Intra-seasonal variability of the abyssal currents in COMRA's contract area in the Clarion-Clipperton Zone. Acta Oceanologica Sinica, 41(11): 1–11, doi: 10.1007/s13131-021-1945-5

1 Introduction

The deep-sea is rich in mineral resources, such as cobalt-rich crusts, rare earth minerals, manganese nodules and combustible ice. With the increasing demand for minerals and metals in social and economic development and the depletion of land resources, interest in exploring seabed mineral resources worldwide is growing. However, the exploration and development of these resources cannot ignore the unique marine ecosystem and environmental problems attached to the habitat. The environmental impact of deep-sea mining activities is a current and cutting-edge issue of international concern. Ocean currents are a dynamic factor that causes plume diffusion in deep-sea mining. To meet the requirements of environmental impact assessments of deep-sea mining, it is first necessary to study the characteristics of deep-sea ocean currents.

Using the deep-sea submarine mooring system, we can obtain the long-term observation data of multilevel hydrological elements such as current, temperature and salinity, which play important roles in the research of deep-sea dynamics. In the eastern part of the Clarion and Clipperton Zone, the moored velocity observations of deep currents near the crest of the East Pacific Rise (9.5°N, 104.3°W) reveal low-frequency variability with characteristic time scales of 1–3 months and maximum speeds up to 10 cm/s (Liang and Thurnherr, 2011). *In situ* observations in the German licence area (12°N, 117°W) show that the low-energy environment more than 4 km below the surface ultimately becomes an order of magnitude more energetic for periods of weeks in response to the passage of mesoscale eddies (Aleynik et al., 2017). In the West Mariana Basin of the western North Pacific (12.5°N, 137°E), significant variations in both currents and temperature within the period of 60 d were found at a depth of approximately 4 000 m and may be associated with the barotropic Rossby wave (Yoshioka et al., 1988). In the Kuroshio Extension region, the moored observations reveal variability with characteristic time scales of 23–38 d for velocity time series and of 38–99 d for temperature time series; whether anticyclonic or cyclonic eddies intensified the deep currents from 2 000 m to 4 000 m in the same direction and increased the amplitude (Liu et al., 2019). In the Philippine Sea (8°N, 127°E), mooring data show an intra-seasonal signal of 60–80 d from the sea surface to the bottom; variations in surface meridional currents along the western boundary of the Pacific Ocean can reach the bottom via low-frequency processes (Wang et al., 2017). Topography is one of the critical controls on deep-ocean dynamics. The presence of sloping topography can derive bottom-trapped topographic Rossby waves (TRWs) which have been observed by field measurements in different ocean basins (Hamilton, 2009; Hamilton et al., 2019; Ma et al., 2019; Oey and Lee, 2002; Shu et al., 2016; Zhu and Liang, 2020). In these measurements, the vertical structure and variability of deep current and/or isotherm displacement conform to TRW theories of intensification with depth and highly vertical coherence throughout the deep-water column. In spite of the fact that TRWs are trapped in deep layer, their energy sources in previous studies are mainly related to upper-ocean forcing, such as

Foundation item: The Fund of China Ocean Mineral Resources R&D Association under contract No. DY135-E2-5-01; the National Program on Global Change and Air-Sea Interaction Ⅱ under contract No. GASI-04-WLHY-01.
*Corresponding author, E-mail: zhangjunpeng@tio.org.cn

the Loop Current and eddies, via potential vorticity adjustment to the changing depth of the bottom or interface (Hamilton, 2009; Hamilton et al., 2019). In other words, observations show that the deep-sea is not calm, and it may be affected by the dynamic process of the upper ocean.

Low-frequency waves in the tropical ocean are important in the study of air-sea interactions in the tropics. Intra-seasonal time scale variations in sea level and current are universal in the tropical ocean (Enfield, 1987; Spillane et al., 1987) and may have close relations with equatorial Kelvin and Rossby waves (Sun and Li, 1998). The period of the most energetic oscillations in the 20–143 d range continuously increases with latitude from approximately 30-d near the tropics to approximately four months near 30°N, in agreement with the latitudinal dependency of the phase speed of westward propagating Rossby waves, which dominate the variability in those latitudes. As a result, the global spatial distributions of the period of the dominant oscillations are largely zonal, with relatively small differences between different ocean basins (Liu et al., 2003; Qiao et al., 2004; Zhai, 2008). However, previous studies on the intra-seasonal variability in the tropical ocean have mainly focused on the upper layers of the ocean. What are the temporal variations of the deep currents? Do they have the same intra-seasonal variability as the upper ocean? These problems remain to be studied.

To obtain the baseline data in the China Ocean Mineral Resources Association (COMRA) polymetallic nodule contact area, which is located in the western part of the area between the Clarion and Clipperton Fraction Zones (CCFZs), we conducted a deep-sea submarine mooring observation in 2017–2018 and obtained direct observation data of the multilevel deep currents for approximately 11 months. The observation data demonstrated significant intra-seasonal variability in deep currents. Therefore, in this paper, the characteristics of intra-seasonal variability of deep currents in the COMRA contract area are systematically studied based on multiple datasets. The possible mechanisms of such intra-seasonal variability are also discussed.

2 Data

2.1 *Field observation*

The subsurface mooring system was deployed at approximately 10°N, 154°W in the deep-sea basin of the COMRA contact area in the western part of the CCFZs of the tropical East Pacific. The mooring anchor was located at a depth of approximately 5 263 m. The global topographic data ETOPO1 show that the water depth of the adjacent area is 4 500–5 500 m (Figs 1a, b). The current data were effectively collected by three 75-kHz acoustic Doppler current profilers (ADCPs) above 1 200 m, two of which were fixed on the float at 300 m and the other was fixed on the float at 800 m. The upward- and downward-looking configurations of the two ADCPs at 300 m were used to cover the range from the sea surface to 800 m depth. The downward-looking configurations of the ADCP at 800 m were used to cover the 800–1 200 m depth range. The gap between the ADCPs was filled by interpolation. The ADCP was separated into 60 bins, with 8 m per bin. The sampling interval of 75-kHz was 1 h. Current meter ob-

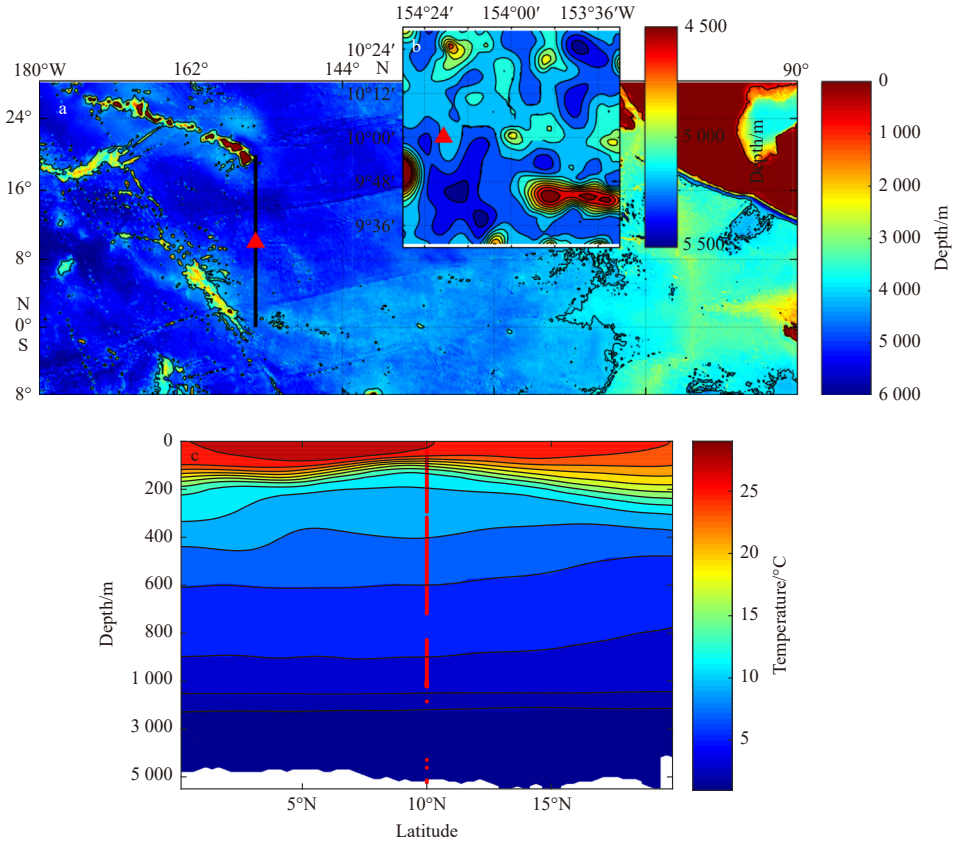

Fig. 1. ETOPO1 depth of the eastern tropical Pacific Ocean, position of the mooring site (red triangle) and the section in c (a); depth around the mooring site (b); climatologic temperature (from World Ocean Atlas 2009) at a meridional section of 154°W (0°–20°N) and the observation range of current metres (red line represents the observation range of 75-kHz ADCPs at upper layers and the red dots below 1 200 m represent the location of Aquadopp current meters) (c).

servations below 1 200 m were collected by five Aquadopp current meters mounted at depths of 1 854 m, 4 292 m, 4 616 m, 5 146 m and 5 223 m. The sampling interval of Aquadopp current meters was 30 min. The observation period lasted for 335 d (September 13, 2017 to August 15, 2018). Figure 1c shows the annual mean temperature at the meridional section of 154°W (0°–20°N). The thermocline depth at the mooring site was 50–200 m, shallower than that on both the northern and southern sides. From the distribution of temperature at the meridional section, it can be inferred that the mooring site is located in the intersection area of the North Equatorial Current and the North Equatorial Counter Current.

2.2 *Other data*

The ECCO2 analysis product is based on a global full-depth ocean and sea ice configuration from the Massachusetts Institute of Technology general circulation model (MIT GCM). The model configuration for this product has a cube-sphere grid with a global horizontal resolution of 0.25° and 50 vertical levels ranging from 10 m thick near the surface to approximately 450 m thick at the deepest level. Green's function approach is used to adjust the control parameters by reducing the model–data misfit (Menemenlis et al., 2005). The data constraints include sea level anomalies from altimeter data; sea surface temperature from the group for high resolution sea surface temperature; and temperature and salinity profiles, including the World Ocean Circulation Experiment TAO, Argo, and expendable bathythermograph (XBT). In this work, we used the solution "cube 92" (version identifier) with a 0.25° regular latitude-longitude grid. The data used in this study span 2000 to 2018 and cover geographic areas of 160°–120°W and 0°–20°N at time intervals of 3 d. This product was downloaded from https://ecco.jpl.nasa.gov/drive/files/ECCO2/cube92_latlon_quart_90S90N.

The OSCAR product is a direct computation of global surface currents using satellite sea surface height, wind, and temperature. Currents are calculated using a quasi-steady geostrophic model together with an eddy viscosity-based wind-driven ageostrophic component and a thermal wind adjustment. This product is in a (1/3)°×(1/3)° Mercator grid at a 5-d time interval and was downloaded from http://apdrc.soest.hawaii.edu/dods/public_data/PODAAC/oscar_local/.

3 Results

3.1 *Periods of the dominant oscillations*

First, 3-d low-pass filtered velocities of selected depth recorded by the 75 kHz ADCPs and current meters, together with the OSCAR surface current, are shown in Fig. 2. It reveals intra-seasonal variability with characteristic time scales of one to three months. Then, the kinetic energy of the intra-seasonal variability (ISV, variations with a period of 20–100 d) and low-frequency variation (variation with a period longer than 20 d) were calculated and are shown in Fig. 3. The kinetic energy of ISV (Ke_isv) and low-frequency (Ke_low) are the time average of kinetic energy through corresponding filtering of zonal and meridional currents. For convenience, we use the layers shallower than 200 m to represent the upper layers, while the layers within 200–1 000 m and under 1 000 m represent the middle layers and deep layers, respectively. Time series of current data are selected at representative depths from 75-kHz ADCPs in the upper 1 200 m and Aquadopp current meters at 1 854 m, 4 292 m, 4 616 m, 5 146 m and 5 223 m, together with the OSCAR surface current during the corresponding time period. As shown in Fig. 3, in general, both Ke_isv and Ke_low decrease with depth. However, Ke_isv and Ke_low present a rise at approximately 4 616 m, the strength of which is close to that at the middle layers. The ratio of Ke_isv to Ke_low increases from less than 30% in the upper layers to over 50% in the deep layer, and its value peaks at 4 616 m is approxim-

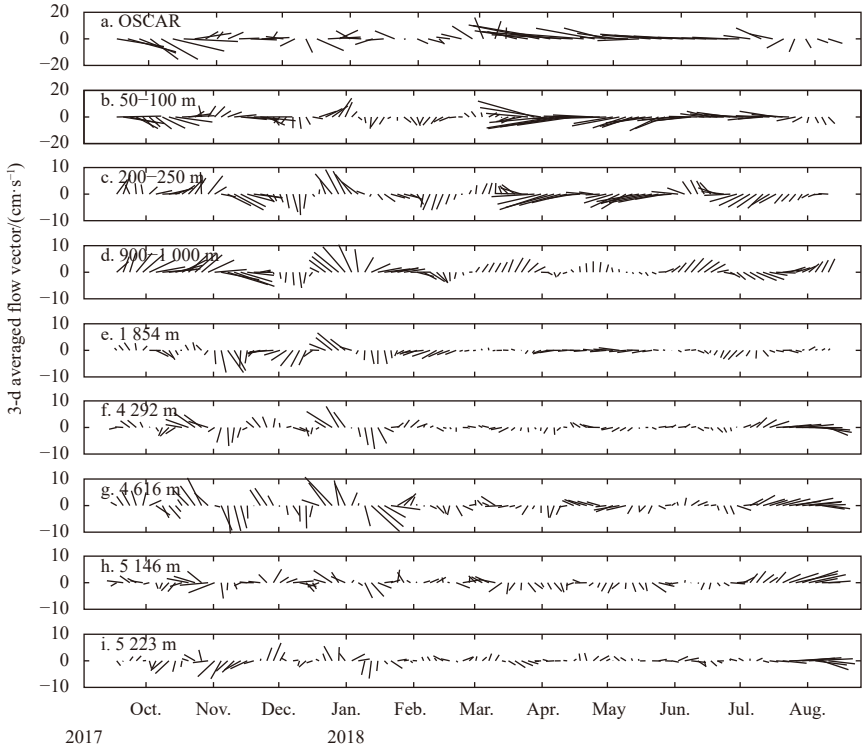

Fig. 2. Time series of 3-d averaged flow vectors after 3-d low-pass filtering at different depths.

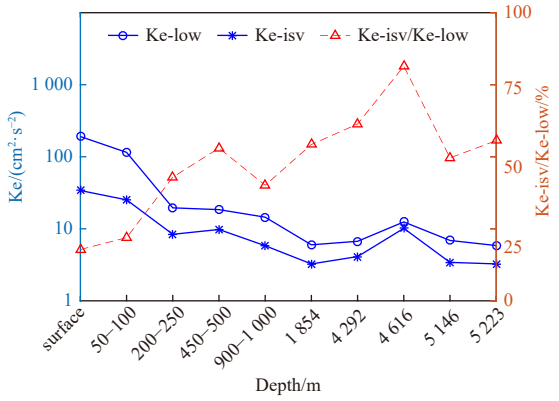

Fig. 3. Kinetic energy of intra-seasonal variability (ISV), low-frequency variability and their ratio. The blue circle line represents kinetic energy of low-frequency variability (Ke-low); the blue asterick line represents kinetic energy of ISV (Ke-isv); the red triangle line represents the ratio of Ke-isv and Ke-low.

ately 80%. As ISV accounts for more than half of the total low-frequency variations in deep layers, we focused on the ISV of deep currents for this study.

To clarify the variability at different depths, the time series measured from 75-kHz ADCPs in the upper 1 200 m and that collected by Aquadopp current meters, together with the surface current, which was used to represent the surface (0 m) current, were processed with a power spectral density (PSD). We divide the intra-seasonal variation into 20–40 d, 40–70 d and 70–100 d to represent the fluctuation with characteristic periods of 1 month, 2 months and 3 months. Figures 4a and b illustrate a uniform peak with a period of 20–120 d at the upper layers in both zonal and meridional currents. However, there was no notable ISV at the middle or deep layers in the zonal direction. For meridional currents, there were consistent 30-d variations at almost all depths, especially at deep layers. In addition, the variations with a period of 2–3 months were also significant at the middle layers.

To analyse the major direction of the ISV of deep currents, the standard deviations of both the meridional and zonal velocities at the intra-seasonal time scale (20–100 d bandpass filtering) were calculated (Fig. 5). The standard deviation of meridional velocity was smaller than that of zonal velocity in the upper layers but greater in the middle layers and most of the deep layers except at 5 146 m. Therefore, we will focus on the ISV of meridional velocity in the following discussions.

3.2 *Temporal variation and vertical structure of ISV of meridional currents*

The temporal variation in the ISV of meridional currents was studied by continuous wavelet transform. The meridional velocity at each representative depth was analysed, and the results are shown in Fig. 6. The period of the most energetic oscillations (referred to as the period of the dominant oscillation below) in the surface and upper layer (50–100 m) is approximately 2 months, showing energetic oscillations from September to March; in addition, there is a 30-d oscillation around January and April (Figs 6a, b). The period of the dominant oscillations of the current in the middle layers (400–450 m and 900–1 000 m) was approximately three months, while in autumn and winter (October to January), a 30-d oscillation was also exhibited (Figs 6c, d). In the deep layers (1 854 m and 4 616 m), the currents showed oscillation characteristics similar to those in the middle layers, and the period of the dominant oscillation was 30 d, with energetic oscillations in autumn and winter (September to February) (Figs 6c, d). The intensity of the 3- and 2-month oscillations decreased with depth, while the intensity of the 30-d oscillation increased with depth. At 4 616 m, the only significant variability was the 30-d oscillation.

The results above show that the ISVs of the middle and deep currents are similar but quite different from those at the upper layers. To further explore the relationship between the deep and upper currents, cross spectrum analysis between the surface meridional current (OSCAR) and those at other depths (mooring) were conducted. Results show that the magnitude of cross-spectral density peaks at the frequency band of ~0.03 counts per day (~30 d) throughout the water column (Fig. 7a), with little phase lag between the surface and deep layers (below 1 000 m, Fig. 7b), indicating that the 30-d oscillation in the deep layers was highly vertical coherence. Significant correlation at the frequency of ~30 d between the surface and deep layers could be inferred from the magnitude-squared coherence as well (Fig. 7c), indicating that the 30-d oscillation in the deep layers was highly correlated with that of surface current.

To display the 30-d variability more directly, the time series of current vectors were drawn after 20–40 d bandpass filtering and 3-d averaging, as shown in Fig. 8. The deep currents showed strong 30-d variations in autumn and winter (October to January), and the oscillations were mainly in the north-northwest and south-southeast directions. The 30-d oscillation below 200 m was basic-

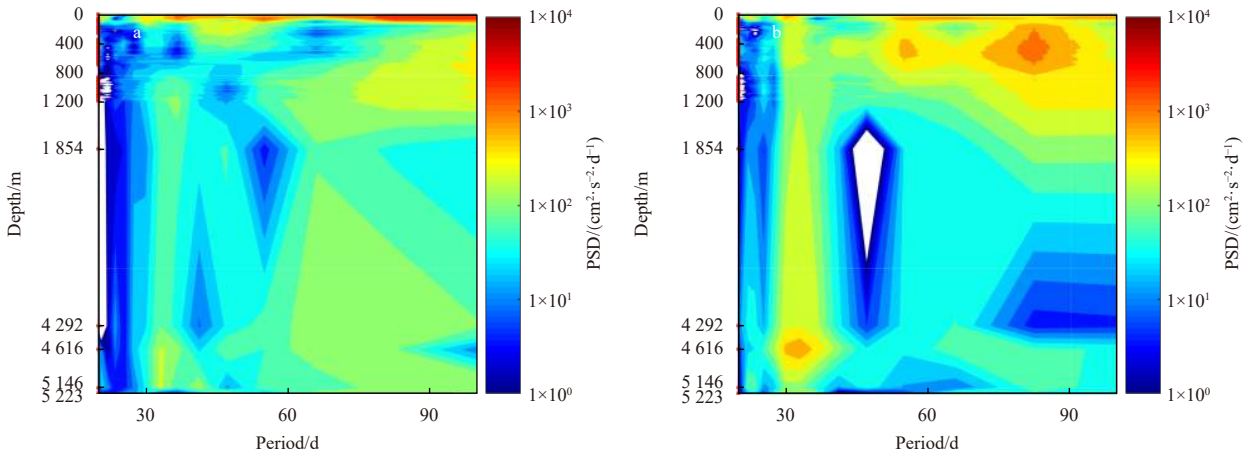

Fig. 4. Power spectral density (PSD) of the velocity in zonal (a) and meridional (b) currents.

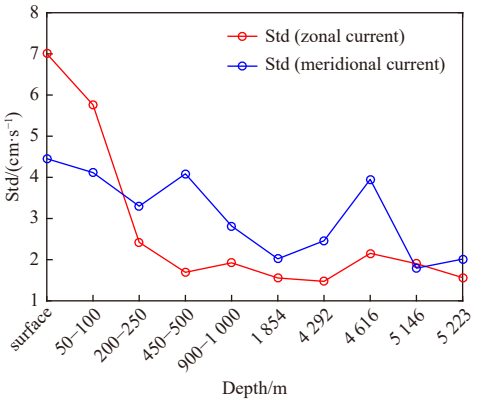

Fig. 5. Standard deviations (Std) of the meridional and zonal velocities at the intra-seasonal time scale.

ally synchronous. The maximum variation was at 4 616 m, and the corresponding velocity was up to 10 cm/s.

3.3 *Propagation features of 30-d oscillation in the deep sea*

The ECCO2 reanalysis product and complex empirical orthogonal function (CEOF, the method was introduced in detail in Oey (2008)) were used to analyse deep 30-d oscillation patterns that can involve propagation. To evaluate the reanalysis data in the deep-sea, the time series of the observed meridional velocities and that extracted from reanalysis data were compared at deep layer (4 616 m). For convenience, the observed data were averaged by three days. Figures 9a and b present the time series and the wavelet coherence spectrum. It shows that the reanalysis data can reproduce the strong oscillation in autumn and winter but obtains an obvious deviation in phase. The wavelet coherence spectrum shows that the two data were highly correlated at the 30-d period, but the phase difference was approximately 90°–150°, indicating that the meridional currents from reanalysis data lead to observations by approximately 7–12 d. Although the phase deviated from the observation, the reanalysis data could reproduce the 30-d oscillation and its time variation. Besides, the power spectral of the meridional velocity at the mooring site shows that the reanalysis data could reproduce the vertical structure of 30-d oscillation as well (Figs 9c and 4b). Thus, we still used the reanalysis data in the following discussion.

The meridional velocity at 4 000 m depth from the reanalysis data was used to examine the propagation features of the 30-d wave in the deep-sea. The data in the region of 160°–120°W, 0°–20°N during the observation period were first filtered through a 20–40 d band-pass filter to obtain the 30-d variation signals, and then the filtered data were used to perform the CEOF analysis. The first CEOF mode could explain 55% of the total variance. The spatial amplitude, phase and reconstructed map, temporal amplitude, phase and spectra of the first CEOF mode were shown in Fig. 10. It showed that an energetic band was along the 4°N, and the most energetic area was located west of 150°W which extended to 12°N (Figs 10a, c). The wave phase propagates westward with zonal wavelengths of 10°–15° of longitude (Fig. 10b), reaching large amplitude during the boreal fall and winter months (Fig. 10d), with a spectra peak at a period about 30 day (Figs 10e, f).

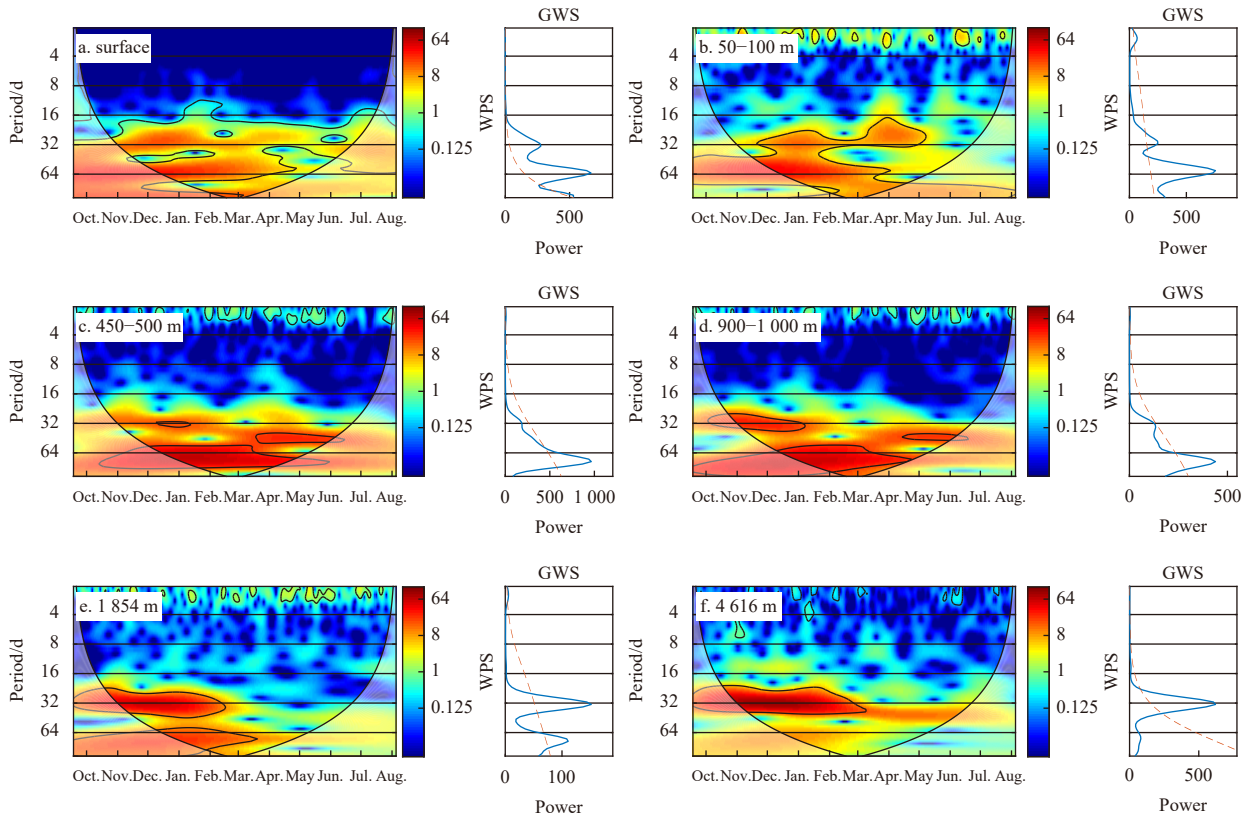

Fig. 6. Continuous wavelet transform of meridional velocity at surface current (a) and currents at 50–100 m (b), 450–500 m (c), 900–1 000 m (d), 1 854 m (e) , 4 616 m (f). The colour filled maps represent the wavelet power spectrum (WPS), and the curves on the right represent the global wavelet spectrum (GWS). In the colour maps, the thick black contours denote the 5% significance level against red noise. The cone of influence where edge effects might distort the picture is shown in lighter shades.

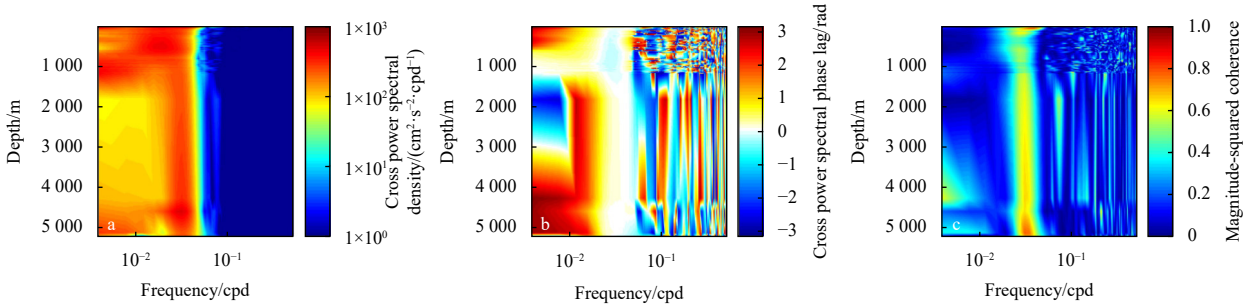

Fig. 7. Cross spectrum analysis between the surface meridional current (OSCAR) and those at other depths. a. Cross power spectral density; b. cross power spectral phase lag; c. magnitude-squared coherence. The cpd means counts per day.

3.4 *Relationship between the 30-d oscillation of deep currents and upper ocean processes*

Tropical instability waves (TIWs) are one of the most prominent features in the equatorial Pacific. The wide range of wavelengths and periods previously reported for TIWs (Qiao and Weisberg, 1995) suggest that there are different instabilities occurring at different wavelengths and periods. The instabilities causing the 30-d spectral peak in sea surface height are sometimes referred to as tropical instability vortices (TIVs) to distinguish them from the shorter-period variability found on the equator (Farrar, 2011). In the Pacific, TIVs usually have periods of 29–36 d and zonal wavelengths of 10°–20° of longitude, appear from boreal summer to winter, located at 3°–8°N, 155°–110°W. TIVs exhibit eddy currents exceeding 70 cm/s, a westward phase propagation speed of about 25–36 km/d, eastward energy propagation. TIWs seem to be contained largely in the surface layer, with energy falling off sharply through the thermocline (Willett et al., 2006). However, a subsurface expression of these waves has been observed through energy propagation into the abyss (Qiao and Weisberg, 1995). Besides, the barotropic Rossby waves are found to be radiated from the TIWs, carrying energy away from the instabilities toward the North Pacific subtropical gyre (Farrar, 2011).

As the 30-d wave in the deep-sea has the same zonal wavelength, frequency, occurrence time and location (Fig. 10) as the tropical instability waves, there may be some kind of relation between the TIWs and the deep 30-d wave. Sea level height data were used to explore the possible relationship between the deep currents and the upper ocean dynamics firstly. The sea level anomaly (SLA) in the region of 0°–20°N, 160°–120°W during the observation period was first 100 d-high-pass filtered to obtain the ISV signals, and then the filtered data were used to conduct the EOF analysis. The spatial patterns and time series of the first three EOF modes are shown in Fig. 11. The total variance contribution of the first three modes was 53%, suggesting that the three modes can explain the major characteristics of ISV. The spatial patterns and time series

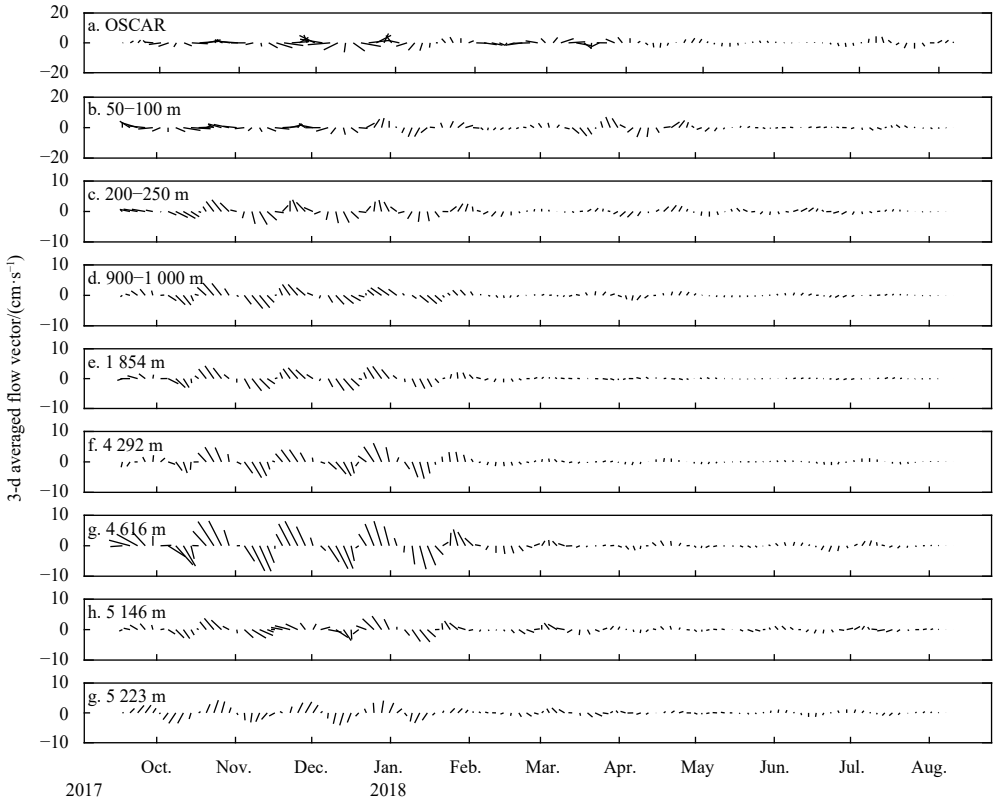

Fig. 8. Time series of 3-d averaged flow vectors after 20–40 d bandpass filtering.

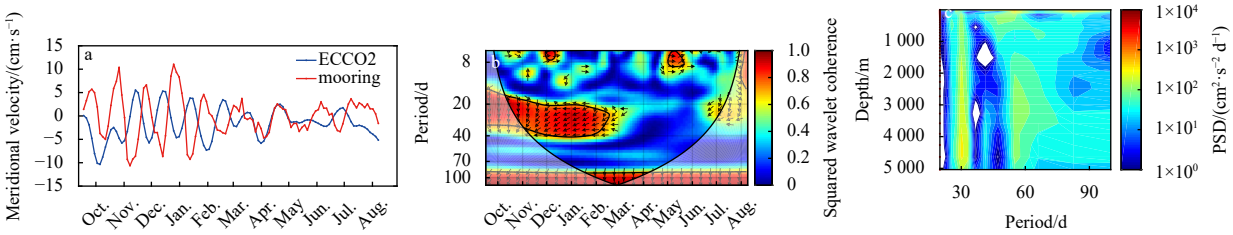

Fig. 9. Comparison of meridional velocity at 4 616 m from observations and reanalysis products. a. Time series; b. squared wavelet coherence; c. power spectral density (PSD) of the meridional velocity at the mooring site, from reanalysis data.

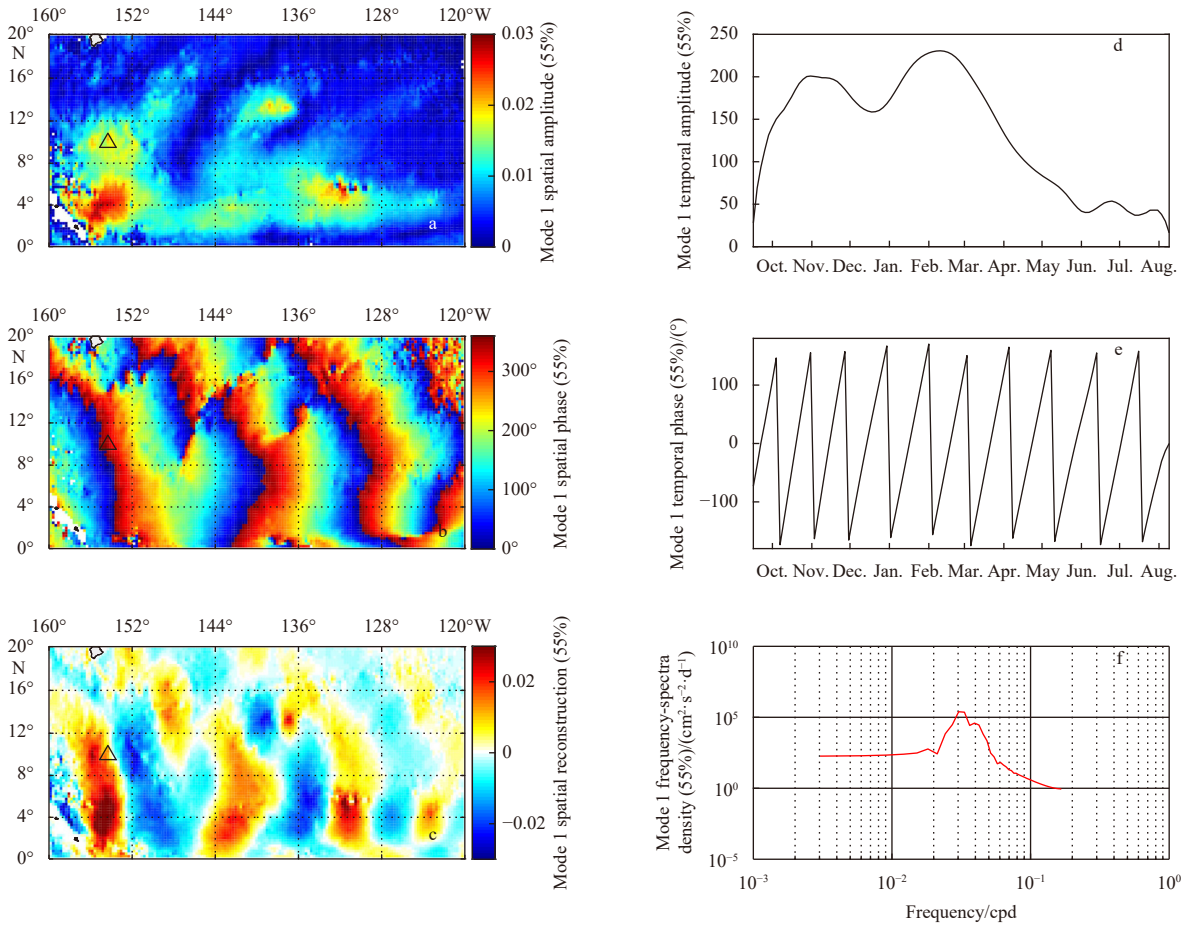

Fig. 10. Spatial amplitude (a), spatial phase (b), spatial reconstruction (c), temporal amplitude (d), temporal phase (e), frequency-spectra density (f) of the first complex empirical orthogonal function (CEOF) mode of meridional velocity at 4 000 m. The mooring site is marked with a triangle in a, b and c. The cpd means counts per day.

of the first two modes were similar, and their cumulative variance contribution was over 46%. The spatial patterns of the first two modes illustrate the eddy pattern centred at 6°N and spanning from 2°N to 10° N, with a wavelength of approximately 1 600 km (13°–15° longitudes). Wavelet analysis revealed that the time series of the first and second modes have similar wavelet spectra, showing energetic oscillations at an approximately 30-d period from autumn to winter (Figs 12a, b). Moreover, the period of the dominant oscillations of the third mode was approximately 2 months (Fig. 12c).

In fact, we found that the spatial distributions and temporal variations of SLA's first two EOF modes (Fig. 11) resembled the characteristics of the TIWs. Therefore, it is suggested that the first and second EOF modes are the TIW patterns, and the time series of the first two EOF modes can be used to represent the temporal variation in TIWs. By comparing the time series of the first EOF mode and the meridional velocity at 4 616 m, the relationship between deep currents and TIWs can be analysed. As shown in Fig. 13a, the time series exhibited similar temporal variations, and their correlation coefficient was up to 0.57. The cross-wavelet analysis and wavelet coherence analysis revealed that there was significant coordinate variation at the 30-d period during autumn and winter, of which the deep currents and TIWs were highly correlated (Figs 13b, c).

To gain further insight into the relationship between upper and deep-sea velocities, we use Singular Value Decomposition (SVD) analysis on upper layer (35 m) and deep layer (4 000 m) meridional velocity from reanalysis product. Figure 14 showed

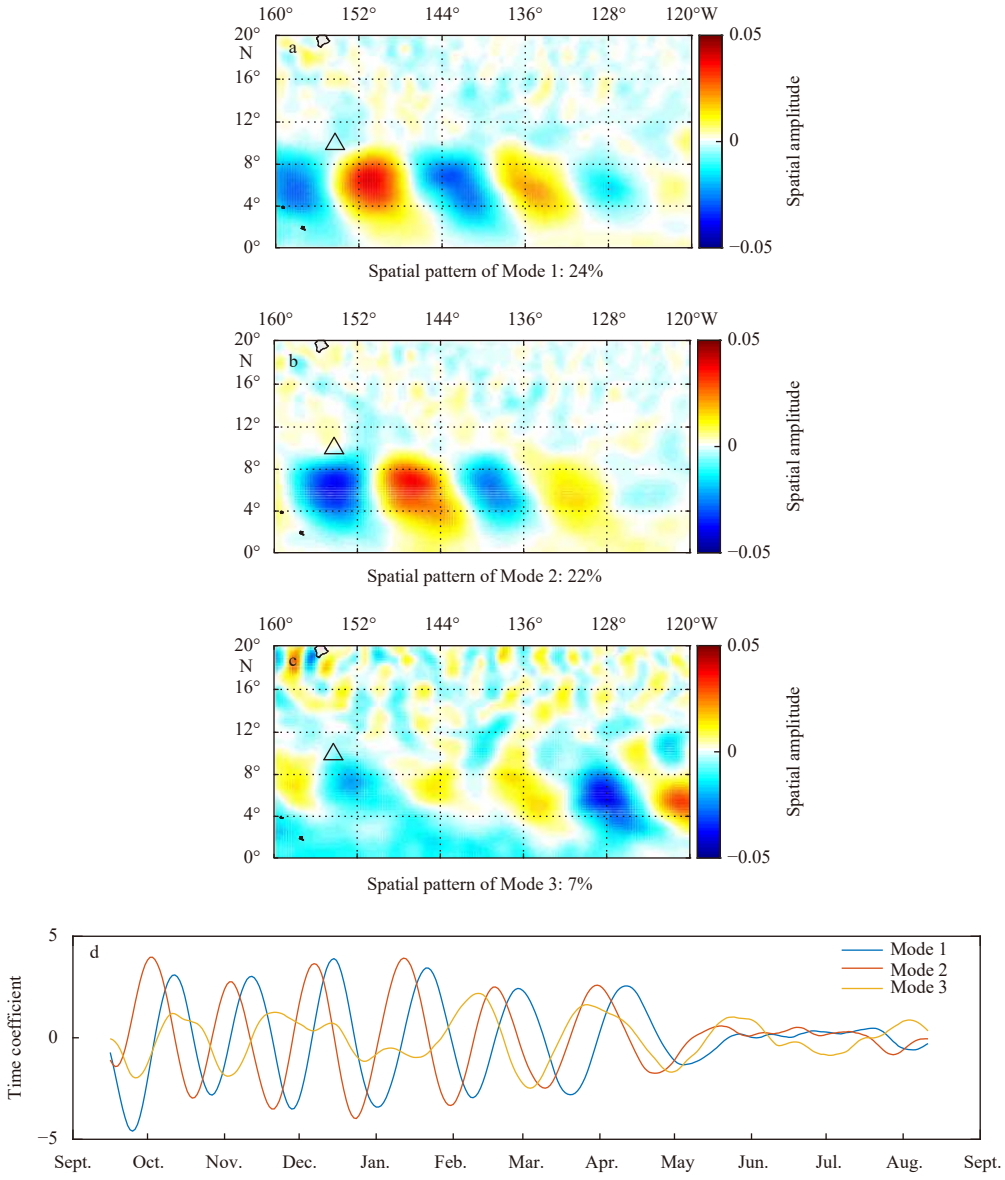

Fig. 11. The first three empirical orthogonal function modes of sea level anomaly at the intra-seasonal time scale.

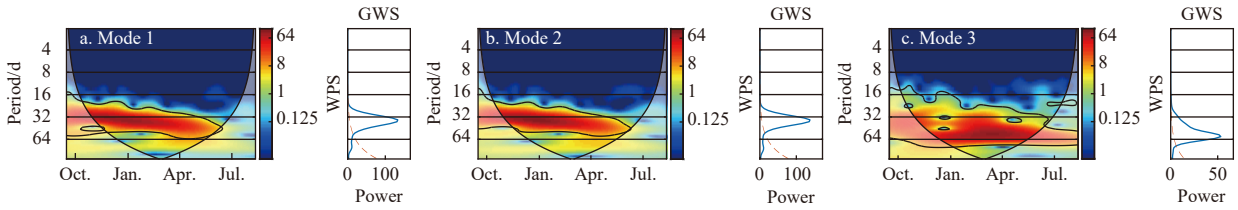

Fig. 12. Continuous wavelet transform of the time series of the first three empirical orthogonal function modes of sea level anomaly. WPS: wavelet power spectrum; GWS: global wavelet spectrum.

the spatial patterns, correlation maps and time series for the first leading SVD mode, which explained 28% of the covariance. The second SVD mode explained 26% of the covariance and had the similar spatial and temporal patterns as Mode 1 except for a phase difference (not shown). The first and second mode explained more than half of the covariance in total. At upper layer, the spatial pattern of the first two modes illustrating the eddy pattern centred at 5°N (Fig. 14a) similar to that of the SLA (Fig. 11a), could be explained as the TIWs pattern. The corresponding spatial pattern at deep layer (Fig. 14b) resembled the first CEOF mode of deep velocity (Figs 10a, c). As shown in the homogeneous and heterogeneous correlation maps, the upper and deep velocity spatial patterns could find to be closely related (Figs 10c, d). The expansion coefficients for the first and second modes are correlated both at 0.92 (significant at 95% level). These high values indicate that deep 30-d oscillation is dominated by changes in the upper ocean.

While the TIWs appear to be confined mainly to the surface

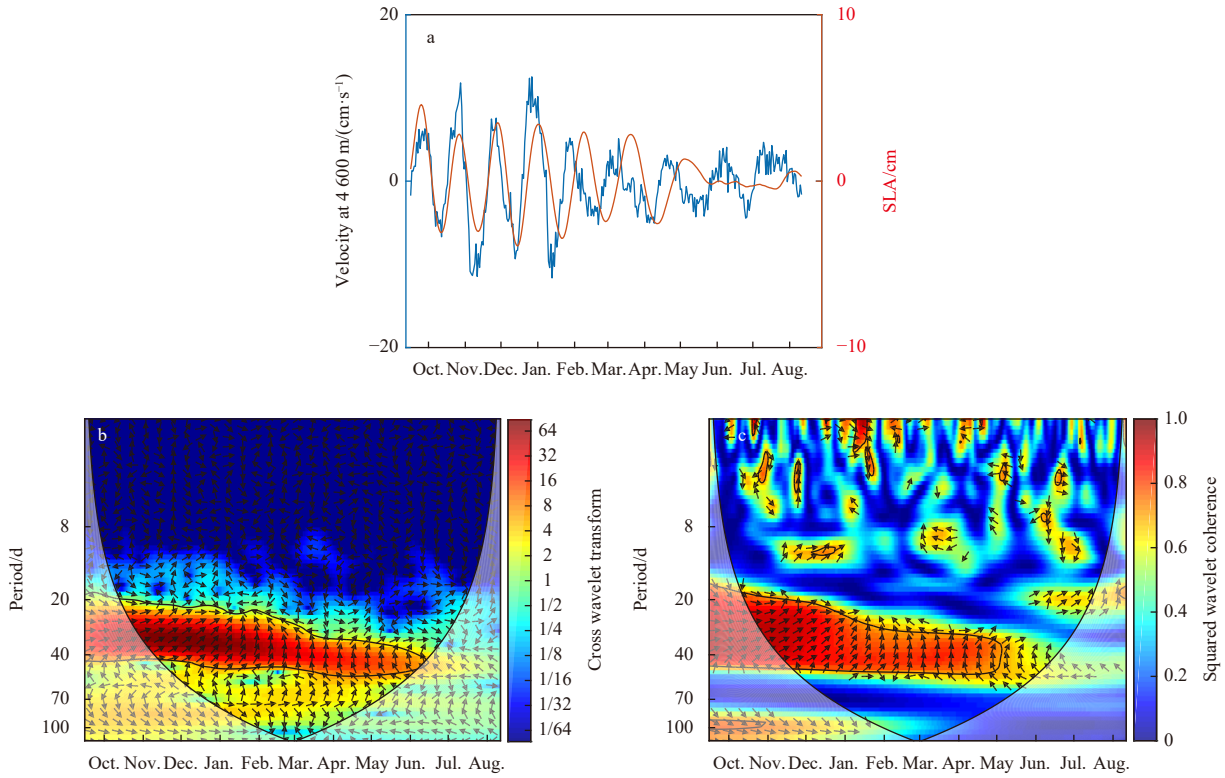

Fig. 13. Time series of the first empirical orthogonal function (EOF) mode of sea level anomaly (SLA) and meridional velocity at 4 616 m (a); cross wavelet transform (b) and squared wavelet coherence (c) between the time series of the first EOF mode of SLA and meridional velocity at 4 616 m.

layer, with energy dropping precipitously through the thermocline, the subsurface expression of these instability waves by energy propagation into the abyss has also been reported (Eriksen, 1985; Eriksen and Richman, 1988; Qiao and Weisberg, 1995). The wave energy generated by instability in the near surface equatorial currents may excite various planetary waves of similar period and wavelength. Internal Rossby-gravity and Rossby waves can carry energy downward and eastward. Vertical radiation by the internal waves is found to provide a significant sink of energy from the surface layers (Cox, 1980). Deep-sea 30-d wave along the 4°N band may be explained by the internal Rossby-gravity and Rossby waves (Figs 10a, c). Different from the upper ocean, the meridional extension could be seen in the deep-sea (Figs 10a, c and 14b) as well. It bears a close resemblance to fields shown in the GCM studies of Cox (1980). Farrar (2011) and Cox (1980) made clear that the variability seen at higher latitudes was a result of the TIWs and that the signal was barotropic. The meridional extension of 30-d wave in the deep-sea in this work may be interpreted as poleward radiation of barotropic Rossby waves from the region of instability as Cox and Farrar's findings.

4 Discussion

In this study, based on direct observation data, ISV accounts for most of the low-frequency variability in the deep sea. At depths below 200 m, the meridional velocity showed a synchronous 30-d oscillation from autumn to winter; the energy of the 30-d oscillation increased with depth and reached a maximum at 4 600 m with a corresponding velocity of approximately 10 cm/s. The 30-d oscillation of deep currents was strongly correlated with the TIWs in the upper ocean.

Amplification of deep current was one the main feature of 30-d oscillation in the observations. A kind of possible explanations was the bottom-trapped TRWs. The observed feature seems to conform to TRWs features of variability intensification with depth and vertical coherence in phase. Under the assumption of $\frac{f\alpha}{H} \gg \beta$, where f is the local Coriolis parameter, α is the topographic slope, H is the water depth, and β is the gradient of f. The linear TRW theory predicts the dispersion relation of

$$\omega \approx -\alpha N \sin\theta, \tag{1}$$

where ω is the TRW frequency, N is buoyancy frequency, and θ is the angle between the wave vector and upslope direction or the angle between the velocity vector and isobaths. In this study, we derived N from the World Ocean Atlas 2013 to be about 6.78×10^{-4} s^{-1} averaged over 3 500–5 000 m, the local slope α was about 0.004 7 (the bathymetry is smoothed first using a 50-km^2 median filter and then fitting smoothing splines to H and α), and f was 2.5×10^{-5} s^{-1} at the mooring site. Because the topography is very complex, θ could not be accurately determined, but it fell in the range between 10° and 20°. The estimated frequency from Eq. (1) was approximately 8.8×10^{-8} Hz to 1.73×10^{-7} Hz, which corresponded to a period of about 67.3–131.5 d, which was larger than the observed period of about 30 d. Additionally, the TRW wavelength is given by

$$\lambda_z = NK/f, \tag{2}$$

where the trapping depth $1/\lambda_z$ can be estimated as the e-folding scale of the TRW amplitude decreasing from the bottom. In this study, we derived it from the first EOF mode of the 30-dmeridional velocity profile from September 15, 2017 to February 1, 2018

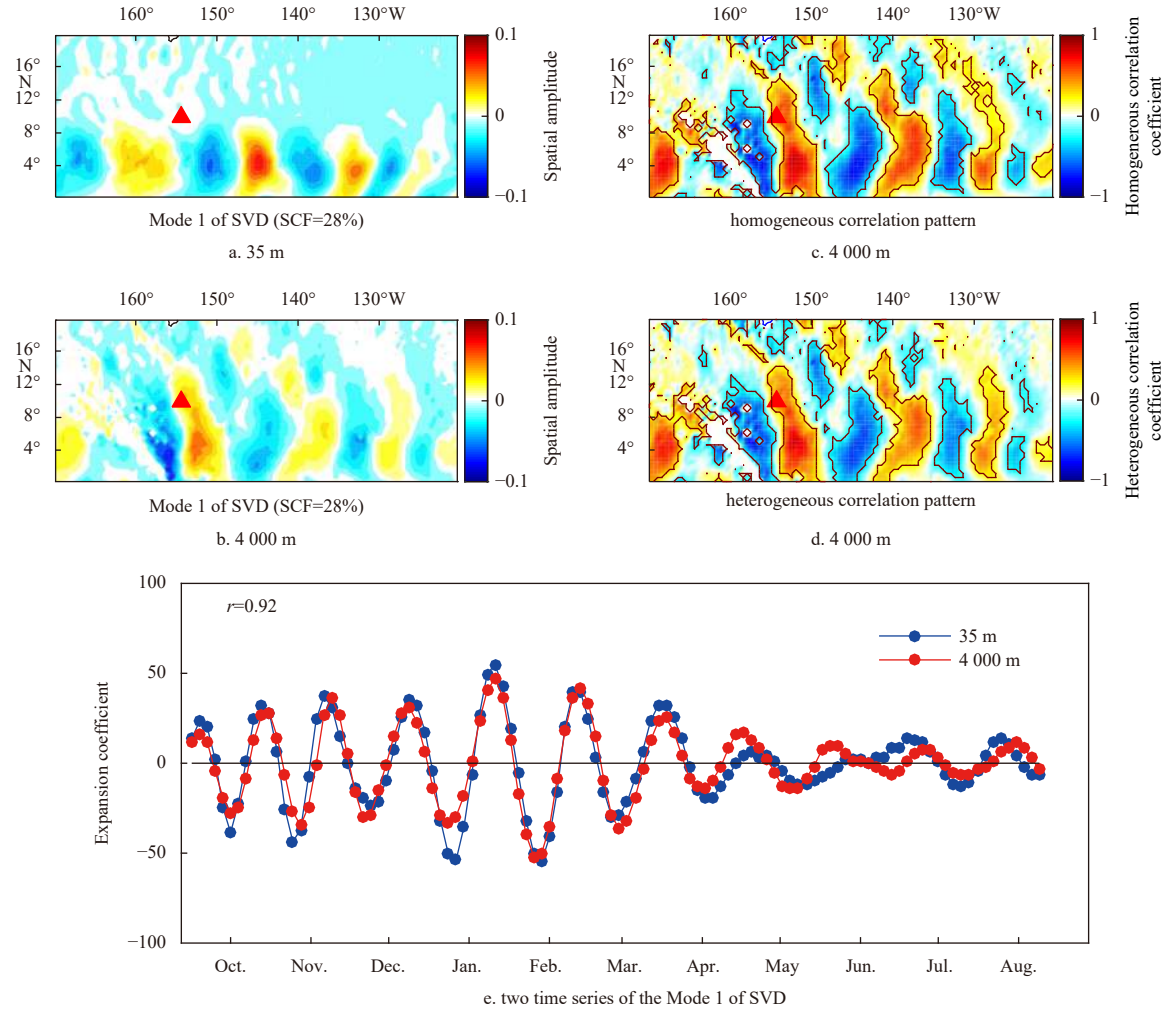

Fig. 14. Spatial patterns of 35 m (a) and 4 000 m (b) meridional velocity; homogeneous (c) and heterogeneous (d) correlation map for the 4 000 m velocity, the 95% significance level is shown as red contours; time evolution of the expansion coefficients of 35 m and 4 000 m meridional velocity (e). All is for the first leading SVD mode. The mooring site is marked with a red triangle in a and b. SVD: Singular Value Decomposition; SCF: Squared Covariance Fraction (measuring the amount of squared covariance for which each mode accounts).

below the depth of 1 000 m. The results showed that the trapping depths were about 3 422 m and 5 022 m from observation and ECCO2, respectively. Based on Eq. (2), the corresponding wavelength was 583–856 km, which seemed not consistent with the previous CEOF analysis (the zonal wavelengths were 10°–15° of longitude). According to the above analysis, it seemed that TRWs could not explain the observed bottom intensification very well. However, we still thought that the bottom intensification may be aroused by some kind of wave-topography interaction (wave reflection and interference et al.). As there was only one mooring with a few vertical samplings in the deep sea, and errors exist in the reanalysis data inevitably, more observations and numerical experiment are needed for further studies of the dynamic mechanism for the bottom intensification.

In this paper, it is stated for the first time that there is a 30-d oscillation in the deep sea, which can lead to an increase in velocity with depth. Such oscillations could last for approximately half of a year and are demonstrated to be closely related to the TIWs in the western part of CCFZs in the tropical East Pacific. The results will provide important information for the environmental impact assessment and prediction of seabed disturbance caused by deep-sea mining.

References

Aleynik D, Inall M E, Dale A, et al. 2017. Impact of remotely generated eddies on plume dispersion at abyssal mining sites in the Pacific. Scientific Reports, 7(1): 16959, doi: 10.1038/s41598-017-16912-2

Cox M D. 1980. Generation and propagation of 30-Day waves in a numerical model of the Pacific. Journal of Physical Oceanography, 10(8): 1168–1186, doi: 10.1175/1520-0485(1980)010<1168:GAPODW>2.0.CO;2

Enfield D B. 1987. The intraseasonal oscillation in eastern Pacific sea levels: how is it forced?. Journal of Physical Oceanography, 17(11): 1860–1876, doi: 10.1175/1520-0485(1987)017<1860:TIOIEP>2.0.CO;2

Eriksen C C. 1985. Moored observations of deep Low-Frequency motions in the central Pacific Ocean: vertical structure and interpretation as equatorial waves. Journal of Physical Oceanography, 15(8): 1085–1113, doi: 10.1175/1520-0485(1985)015<1085:MOODLF>2.0.CO;2

Eriksen C C, Richman J. 1988. An estimate of equatorial wave energy flux at 9- to 90-day periods in the Central Pacific. Journal of Geophysical Research: Oceans, 93(C12): 15455–15466, doi: 10.1029/JC093iC12p15455

Farrar J T. 2011. Barotropic Rossby waves radiating from tropical instability waves in the Pacific Ocean. Journal of Physical Oceanography, 41(6): 1160–1181, doi: 10.1175/2011JPO4547.1

Hamilton P. 2009. Topographic Rossby waves in the Gulf of Mexico. Progress in Oceanography, 82(1): 1–31, doi: 10.1016/j.pocean.2009.04.019

Hamilton P, Bower A, Furey H, et al. 2019. The loop current: observations of deep eddies and topographic waves. Journal of Physical Oceanography, 49(6): 1463–1483, doi: 10.1175/JPO-D-18-0213.1

Liang Xinfeng, Thurnherr A M. 2011. Subinertial variability in the deep ocean near the East Pacific Rise between 9° and 10°N. Geophysical Research Letters, 38(6): L06606

Liu Qinyu, Pan Aijun, Liu Zhengyu. 2003. Intraseasonal oscillation and baroclinic instability of upper layer ocean in the north equator current. Oceanologia et Limnologia Sinica, 34(1): 94–100

Liu Yansong, Yu Fei, Nan Feng, et al. 2019. Intraseasonal oscillation of deep currents influenced by mesoscale eddies in the Kuroshio Extension Region. Scientific Reports, 9(1): 4147, doi: 10.1038/s41598-019-39567-7

Ma Qiang, Wang Fan, Wang Jianing, et al. 2019. Intensified deep ocean variability induced by topographic rossby waves at the Pacific Yap-Mariana junction. Journal of Geophysical Research: Oceans, 124(11): 8360–8374, doi: 10.1029/2019JC015490

Menemenlis D, Fukumori I, Lee T. 2005. Using green's functions to calibrate an ocean general circulation model. Monthly Weather Review, 133(5): 1224–1240, doi: 10.1175/MWR2912.1

Oey L Y. 2008. Loop current and deep eddies. Journal of Physical Oceanography, 38(7): 1426–1449, doi: 10.1175/2007JPO3818.1

Oey L Y, Lee H C. 2002. Deep eddy energy and topographic Rossby waves in the Gulf of Mexico. Journal of Physical Oceanography, 32(12): 3499–3527, doi: 10.1175/1520-0485(2002)032<3499:DEEATR>2.0.CO;2

Qiao Fangli, Tal E, Yuan Yeli. 2004. The zonal distribution features of high frequency oscillations in the oceans derived from satellite altimeter data. Haiyang Xuebao (in Chinese), 26(3): 1–7

Qiao L, Weisberg R H. 1995. Tropical instability wave kinematics: observations from the Tropical Instability Wave Experiment. Journal of Geophysical Research: Oceans, 100(C5): 8677–8693, doi: 10.1029/95JC00305

Shu Yeqiang, Xue Huijie, Wang Dongxiao, et al. 2016. Persistent and energetic bottom-trapped topographic Rossby waves observed in the southern South China Sea. Scientific Reports, 6(1): 24338, doi: 10.1038/srep24338

Spillane M C, Enfield D B, Allen J S. 1987. Intraseasonal oscillations in sea level along the west coast of the Americas. Journal of Physical Oceanography, 17(3): 313–325, doi: 10.1175/1520-0485(1987)017<0313:IOISLA>2.0.CO;2

Sun Jilin, Li Li. 1998. Priliminary analysis on Lower Frequency Waves in the Equatorial Pacific. Journal of Ocean University of Qingdao, (3): 24–30

Wang Fujun, Zhang Linlin, Hu Dunxin, et al. 2017. The vertical structure and variability of the western boundary currents east of the Philippines: case study from *in situ* observations from December 2010 to August 2014. Journal of Oceanography, 73(6): 743–758, doi: 10.1007/s10872-017-0429-x

Willett C S, Leben R R, Lavín M F. 2006. Eddies and Tropical Instability Waves in the eastern tropical Pacific: a review. Progress in Oceanography, 69(1–2): 218–238

Yoshioka N, Endoh M, Ishizaki H. 1988. Observation of the abyssal current in the West Mariana Basin. Journal of the Oceanographical Society of Japan, 44(1): 33–39, doi: 10.1007/BF02303148

Zhai Ping. 2008. The distribution characteristic and mechanism of intraseasonal oscillations in global oceans (in Chinese) [dissertation]. Qingdao: Ocean University of China

Zhu Yingli, Liang Xinfeng. 2020. Coupling of the surface and Near-Bottom currents in the Gulf of Mexico. Journal of Geophysical Research: Oceans, 125(11): e2020JC016488